A Correlation Analysis of Field Potential and Action Potential Biomarkers in Heterogeneous hiPSC-Derived Cardiac Tissues

Sofia Botti

sofia.botti@polimi.it

Università della Svizzera Italiana

Marco Favino

Università della Svizzera Italiana

Rolf Krause

King Abdullah University of Science and Technology

Claudia Altomare

Ente Ospedaliero Cantonale

Lucio Barile

Ente Ospedaliero Cantonale

Article

Keywords:

Posted Date: June 2nd, 2026

DOI: https://doi.org/10.21203/rs.3.rs-9787691/v1

Additional Declarations: No competing interests reported.

A Correlation Analysis of Field Potential and Action Potential Biomarkers in Heterogeneous hiPSC-Derived Cardiac Tissues

A Preprint

S. Botti[*], Euler Institute, Faculty of Informatics, Università della Svizzera Italiana, Lugano, CH
M. Favino, Euler Institute, Faculty of Informatics, Università della Svizzera Italiana, Lugano, CH
R. Krause, AMCS, CEMSE, King Abdullah University of Science and Technology, Thuwal, Kingdom of Saudi Arabia
C. Altomare, Cardiovascular Theranostics, Istituto Cardiocentro Ticino, Ente Ospedaliero Cantonale, Lugano, CH
L. Barile, Cardiovascular Theranostics, Istituto Cardiocentro Ticino, Ente Ospedaliero Cantonale, Lugano, CH

May 15, 2026

Abstract

Human induced pluripotent stem cell–derived cardiomyocytes (hiPSC-CMs) provide a powerful platform for investigating human cardiac electrophysiology and for supporting safety pharmacology studies. However, their intrinsic heterogeneity, typically involving mixtures of atrial-like and ventricular-like phenotypes, and the indirect nature of multielectrode array (MEA) recordings make the interpretation of Field Potential (FP) biomarkers challenging. A quantitative understanding of how MEA-derived metrics reflect the underlying action potential dynamics, which represent the gold standard, is still limited but essential for establishing robust and translatable *in-vitro* readouts. In this work, we present a computational framework that couples the bidomain model with a detailed representation of MEA electrodes to perform an *in-silico* correlation study between FP and action potential based electrophysiological biomarkers in heterogeneous hiPSC-CM tissues. We first analyze a large set of 900 spatially distributed sampling points to explore the relationship between extracellular potentials and their corresponding cellular action potential features across varying mixtures of atrial-like and ventricular-like cells. We then simulate a full MEA platform comprising 256 electrodes to assess how realistic subsampling, spatial organization, and tissue composition affect the extraction and interpretation of FP biomarkers. Across a broad panel of biomarkers, our results identify the FP metrics that most reliably reflect action potential characteristics and demonstrate that the strength of field-action potential correlations increases as the tissue exhibits a more homogeneous ventricular-like phenotype. These findings not only clarify the mechanistic basis of MEA readouts in hiPSC-CM systems but also highlight the predictive potential of our computational tool. By integrating tissue composition, spatial sampling, and electrophysiological modeling, the framework can serve as a virtual platform to anticipate biomarker behavior, optimize MEA-based experimental designs, and ultimately strengthen the translational value of hiPSC-CM assays in preclinical research.

Introduction

Human induced pluripotent stem cell–derived cardiomyocytes (hiPSC-CMs) have emerged as a central platform for cardiac disease investigation and drug safety assessment [15, 25]. By enabling patient-specific investigations in a

[*]sofiabotti95@gmail.com - sofia.botti@polimi.it

controlled *in-vitro* environment, hiPSC-CMs provide ethically sustainable and scalable alternatives to animal models and clinical studies. Their integration with multi-electrode array (MEA) systems further allows non-invasive and high-throughput recordings of extracellular electrical activity, namely the field potential (FP), making hiPSC-CM monolayers a cornerstone technology in contemporary preclinical cardiology, [19, 21, 23, 26]. Despite these advantages, hiPSC-CM preparations often include cells at different maturation stages, with incomplete differentiation and mixed electrophysiological phenotypes. This cellular heterogeneity remains a major challenge for the interpretation and standardization of MEA-derived biomarkers [13].

In MEA experiments, cardiac repolarization is typically quantified using FP duration (FPD) or derived biomarkers, related to the extracellular potential, which are commonly interpreted as surrogates for action potential duration (APD), [11, 20]. While such biomarkers have proven effective in relatively homogeneous experimental settings, their reliability in heterogeneous tissues—where atrial-like (AL) and ventricular-like (VL) hiPSC-CMs coexist—is still an open question. In particular, extracellular recordings intrinsically involve spatial averaging, as each MEA electrode integrates signals from multiple cells within its sensing region. When different cellular phenotypes are present, this mixing effect may substantially alter the relationship between intracellular electrophysiological properties and the recorded FP signals.

The interpretation of MEA-derived biomarkers is inherently a multiscale problem. Intracellular ionic dynamics determine the shape and duration of the single-cell AP, while electrical propagation across the tissue and the electrode–tissue coupling mechanisms shape the extracellular signals detected by the MEA. Experimentally disentangling these contributions is particularly challenging in heterogeneous tissues, which motivates the use of computational modeling as a controlled and reproducible framework to systematically investigate the relationship between AP- and FP-based biomarkers.

In this work, we present a comprehensive *in-silico* investigation of the relationship between intracellular AP biomarkers and extracellular MEA-derived markers in heterogeneous hiPSC-CM tissues. We employ a two-dimensional bidomain model [5] explicitly coupled with a multichannel MEA approximation (i.e. a system the electrodes dynamic) to simulate from cardiac monolayers both the point-wise defined extracellular potential and the electrode FP recordings [1, 3]. The simulated tissues consist of mixtures of VL and AL phenotypes, enabling the controlled investigation of phenotypic heterogeneity. VL cells are described by the Paci2020 ionic model [17], while AL cells are modeled using the atrial-specific Botti2024 formulation [4], allowing us to reproduce key differences in repolarization dynamics and conduction properties between the two phenotypes.

By systematically varying the degree of tissue heterogeneity and analyzing multiple duration-based biomarkers, we quantify the strength of the relationship between intracellular AP features and their extracellular counterparts. Particular attention is devoted to the comparison between biomarkers derived from extracellular potential, sampled at the tissue level, and FP signals recorded at MEA electrodes, highlighting the role of spatial averaging and phenotypic mixing in shaping biomarker reliability. In addition, we investigate the behavior of advanced repolarization descriptors, such as $\mathrm{APD}_{20/90}$ [2], and analyze the effect of pharmacological modulation through 4-aminopyridine, providing further insight into phenotype-specific responses in heterogeneous tissues.

Overall, this study aims to clarify under which conditions MEA-derived biomarkers can be reliably interpreted as indicators of intracellular electrophysiological dynamics. By combining detailed ionic models with explicit simulations of MEA recordings, our work provides a quantitative framework for linking cellular electrophysiology to experimentally observable signals, contributing to the development of more robust and mechanistically grounded tools for cardiac drug testing and electrophysiological characterization of hiPSC-CM preparations.

Materials and methods

The cardiac MEA model

In cardiac electrophysiology, the bidomain model describes cardiac tissue as a continuum composed of two superimposed conductive media, corresponding to the intracellular and extracellular spaces [16, 28]. The electrical state of the tissue, for $\boldsymbol{x} \in \Omega$ and $t \in (0, T)$, is characterized by the intracellular and extracellular potentials, u_i and u_e, whose difference defines the transmembrane potential

$$v(\boldsymbol{x}, t) = u_i(\boldsymbol{x}, t) - u_e(\boldsymbol{x}, t). \tag{1}$$

The two media are coupled through the cellular membrane via ionic currents, which depend on the transmembrane potential and additional state variables describing the cellular electrophysiological dynamics. Charge conservation then leads to the bidomain equations; we refer to [5, 24] for a detailed derivation.

To account for electrode measurements, the model is augmented following [1]. Let e_k denote the surface of the k^{th} electrode. The current I^k recorded by the electrode satisfies

$$\frac{dI^k}{dt} + \frac{I^k}{\tau} = \frac{C_{\text{el}}}{\tau}\frac{dU^k}{dt}, \quad \text{with} \quad U^k = \frac{1}{|e_k|}\int_{e_k} u_e \, \mathrm{d}e_k, \tag{2}$$

where $\tau = (R_i + R_{\text{el}})C_{\text{el}}$, with R_i the resistance to ground and R_{el}, C_{el} the electrode resistance and capacitance, respectively.

On each electrode surface e_k, the extracellular potential satisfies the boundary condition [14]

$$\mathrm{D}_e \nabla u_e \cdot \mathbf{n} = \frac{I^k}{|e_k|}. \tag{3}$$

Assuming that the thickness z_{thick} of the cell monolayer is negligible compared to the in-plane dimensions, variations along the orthogonal direction can be neglected, leading to an effective two-dimensional formulation. Under this approximation, Eq. (3) can be rewritten as a volumetric source term in the bidomain equations. The FP measured by the k^{th} electrode is defined as

$$U^k_{\text{FP}} = R_i I^k. \tag{4}$$

The resulting MEA model in parabolic–elliptic form reads

$$\begin{cases} \chi C_m \dfrac{\partial v}{\partial t} - \operatorname{div}(\mathrm{D}_i \nabla v) - \operatorname{div}(\mathrm{D}_i \nabla u_e) + \chi I_{\text{ion}}(v, \boldsymbol{w}, \boldsymbol{c}) = 0 & \text{in } \Omega \times (0,T) \quad \text{(5a)} \\ -\operatorname{div}(\mathrm{D}_i \nabla v) - \operatorname{div}((\mathrm{D}_i + \mathrm{D}_e)\nabla u_e) = \dfrac{1}{z_{\text{thick}}} \displaystyle\sum_{e_k} \frac{I^k}{|e_k|}\chi_{e_k} & \text{in } \Omega \times (0,T) \quad \text{(5b)} \\ \dfrac{dI^k}{dt} + \dfrac{I^k}{\tau} = \dfrac{C_{\text{el}}}{\tau}\dfrac{dU^k}{dt}, \quad U^k = \dfrac{1}{|e_k|}\displaystyle\int_{e_k} u_e \, \mathrm{d}e_k & \text{on } e_k \times (0,T) \quad \text{(5c)} \\ \dfrac{d\boldsymbol{w}}{dt} = \boldsymbol{F}(v, \boldsymbol{w}, \boldsymbol{c}), \qquad \dfrac{d\boldsymbol{c}}{dt} = \boldsymbol{G}(v, \boldsymbol{w}, \boldsymbol{c}) & \text{in } \Omega \times (0,T) \quad \text{(5d)} \end{cases}$$

where $|e_k|$ denotes the surface of the k^{th} electrode and χ_{e_k} its characteristic function.

This formulation explicitly couples tissue electrophysiology with electrode dynamics, allowing the direct simulation of field potentials recorded by MEA systems.

This formulation explicitly couples tissue electrophysiology with electrode dynamics, allowing the direct simulation of FPs recorded by MEA systems, in contrast with organ-scale bidomain simulations where electrode signals are typically reconstructed through pseudo-ECG or lead-field approaches [7].

The system also embeds the single-cell ionic model through the transmembrane ionic current $I_{\text{ion}} = I_{\text{ion}}(v, \boldsymbol{w}, \boldsymbol{c})$, which reproduces the electrophysiological behavior of hiPSC-derived cardiomyocytes. This includes the dynamics of multiple transmembrane ionic channels together with intracellular calcium (Ca^{2+}) regulation, described by the system of ordinary differential equations in Eq. (5d). The vector $\boldsymbol{w}$ collects the gating variables $w^1, \ldots, w^s$, while $\boldsymbol{c}$ represents the vector of ionic concentrations, specifically c^1, c^2, c^3.

The system is coupled with the following initial conditions for the transmembrane potential, gating variables, and ionic concentrations

$$v(\boldsymbol{x}, 0) = v_0, \qquad \boldsymbol{w}(\boldsymbol{x}, 0) = \boldsymbol{w_0}, \qquad \boldsymbol{c}(\boldsymbol{x}, 0) = \boldsymbol{c_0}. \tag{6}$$

and by the boundary conditions

$$\text{D}_i \nabla(v + u_e) \cdot \mathbf{n} = 0 \qquad \text{on } \partial\Omega \times (0, T) \tag{7a}$$

$$\text{D}_e \nabla u_e \cdot \mathbf{n} = 0 \qquad \text{on } \partial\Omega_N \times (0, T) \tag{7b}$$

$$u_e = 0 \qquad \text{on } \partial\Omega_D \times (0, T) \tag{7c}$$

where $\partial\Omega = \partial\Omega_N \cup \partial\Omega_D$ with $\partial\Omega_N \cap \partial\Omega_D = \emptyset$. Here $\partial\Omega_N$ and $\partial\Omega_D$ denote the portions of the boundary where Neumann and Dirichlet conditions are imposed, respectively. In particular, $\partial\Omega_D$ is introduced to enforce grounding, i.e., to simulate the electrode system being connected to ground on three sides of the computational domain.

Tissue conductivity. In adult cardiac tissue, the arrangement of fibers rotating from epicardium to endocardium promotes electrical propagation along preferred directions.

Since maturation affects conductivity in a manner that is difficult to quantify experimentally and no clear preferential direction is typically observed in hiPSC-derived cardiomyocyte monolayers, we consider an axisymmetric isotropic medium. The conductivity tensors are therefore defined as

$$\text{D}_i = \sigma_i \mathbf{I}, \qquad \text{D}_e = \sigma_e \mathbf{I}. \tag{8}$$

We choose $\sigma_i = 0.7875\,\text{mS/cm}$ and $\sigma_e = 0.3375\,\text{mS/cm}$, yielding an average conduction velocity of approximately $11.5\,\text{cm/s}$ in the homogeneous configuration. These values are lower than those typically reported for adult human cardiac tissue, reflecting the slower electrical propagation observed in hiPSC-derived cardiomyocytes.

Stimulation protocol. Electrical activation of the tissue was initiated by applying an external stimulus current I_{app} localized in a square region of side $0.2\,\text{mm}$ positioned at one corner of the computational domain. The stimulus consisted of a rectangular pulse with amplitude $I_{\text{app}} = 280\,\mu\text{A/cm}^2$ and duration $t_{\text{app}} = 0.3\,\text{ms}$.

In experimental settings, hiPSC-derived cardiomyocytes possess intrinsic spontaneous electrophysiological activity and do not require external pacing to sustain rhythmic beating. In the simulation, a single stimulus pulse was applied at the beginning to define a spatially localized activation site and trigger deterministic wave propagation; no further external stimulation was imposed thereafter. The tissue subsequently maintained self-organized rhythmic beating, relying entirely on the spontaneous electrophysiological properties intrinsic to these cells.

Each simulation was run for a total duration of $4.1\,\text{s}$, allowing transient dynamics to decay and enabling the analysis of stable beating cycles.

Tissue heterogeneity and ionic phenotypes

To account for this experimentally observed variability, tissue heterogeneity was explicitly introduced in the computational domain by combining VL and AL hiPSC-CMs within the same simulated tissue. Four heterogeneous configurations were considered, corresponding to increasing fractions of AL cells: 0% (homogeneous VL tissue), 10%, 20%, and 30% AL hiPSC-CMs. In each configuration, AL cells were randomly distributed across the discretized

domain, while the remaining fraction was assigned a VL phenotype. The random distribution of the heterogeneity patterns is illustrated in the first column of Figure 3.

The upper bound of 30% AL cells was selected based on experimental observations indicating that, in standard differentiation protocol [2], the proportion of AL cells rarely exceeds this value. Moreover, larger atrial fractions would significantly alter the morphology of extracellular and FP signals, which are primarily characterized and validated for VL electrophysiology. For this reason, only heterogeneous configurations within this physiologically relevant range were considered.

Consistently with MEA experimental conditions, electrical activation of the tissue was initiated from a localized region composed exclusively of VL hiPSC-CMs.

At the single-cell level, several ionic models have been proposed to describe hiPSC-CMs, including VL formulations [9, 10, 18, 22] and more recent atrial-specific models [4]. In this work, the VL phenotype was modeled using the Paci2020 hiPSC-CM ionic model [17], which reproduces both spontaneous activity and stimulus-induced APs typical of VL hiPSC-CMs. The AL phenotype was modelled using the atrial-specific ionic model introduced in [4]. To better reproduce the immature electrophysiological behavior observed in hiPSC-CM cultures, a modified version of the atrial model was employed by adjusting selected ionic conductances ($g_{K1} = 0.06\,\mathrm{nS}/\mu\mathrm{F}$ with respect to $g_{K1} = 0.169\,\mathrm{nS}/\mu\mathrm{F}$ in the original model), allowing the model to reproduce both spontaneous firing activity and paced responses.

By combining spatially distributed ionic phenotypes with a shared bidomain and MEA formulation, the proposed modeling framework enables the systematic investigation of how tissue-level heterogeneity influences extracellular and FP biomarkers and how reliably these markers reflect the underlying transmembrane AP dynamics.

Computational domain

The computational domain Ω represents a cardiac tissue layer coupled with a multichannel MEA system composed of 256 circular electrodes. All electrodes have identical geometry, with a diameter of $30\,\mu m$, and the inter-electrode spacing is $200\,\mu m$. The electrodes are arranged in a uniform square grid, see Figure 1.

Unlike standard multiwell systems, the present setup consists of a single continuous domain without physical wells, allowing the simulation of a homogeneous tissue sheet interacting simultaneously with all electrodes.

The modeled tissue has a square shape with side length equal to 6 mm, fully covering the active electrode area of the MEA. The electrode array is centered within the domain, ensuring symmetric boundary conditions and a uniform spatial distribution of recording sites. Each electrode is modeled as a circular surface embedded in the extracellular domain, maintaining constant radius and inter-electrode distance across the array.

The domain is discretized using a structured Cartesian mesh of quadrilateral elements, refined to accurately resolve both the electrode boundaries and the electrical field variations within the tissue. This setup provides a realistic representation of the MEA–tissue interaction in a large-scale multichannel configuration suitable for high-resolution numerical investigations.

Numerical methods

The MEA bidomain system was spatially discretized using first-order isoparametric finite elements on a structured square mesh composed of 400×400 elements. The resulting mesh size is $h = 1.5\,\mu\mathrm{m}$, leading to a total of 160.801 mesh nodes for each scalar field defined over the computational domain.

The mesh resolution was specifically designed to match the geometrical dimensions of the electrodes. Given the very fine discretization, each electrode area is directly represented and approximated by mesh elements, without requiring geometrical interpolation of the extracellular potential over the electrode surface. Electrode integrals can therefore be computed through simple element-wise averaging, reducing approximation errors in the evaluation of FP signals.

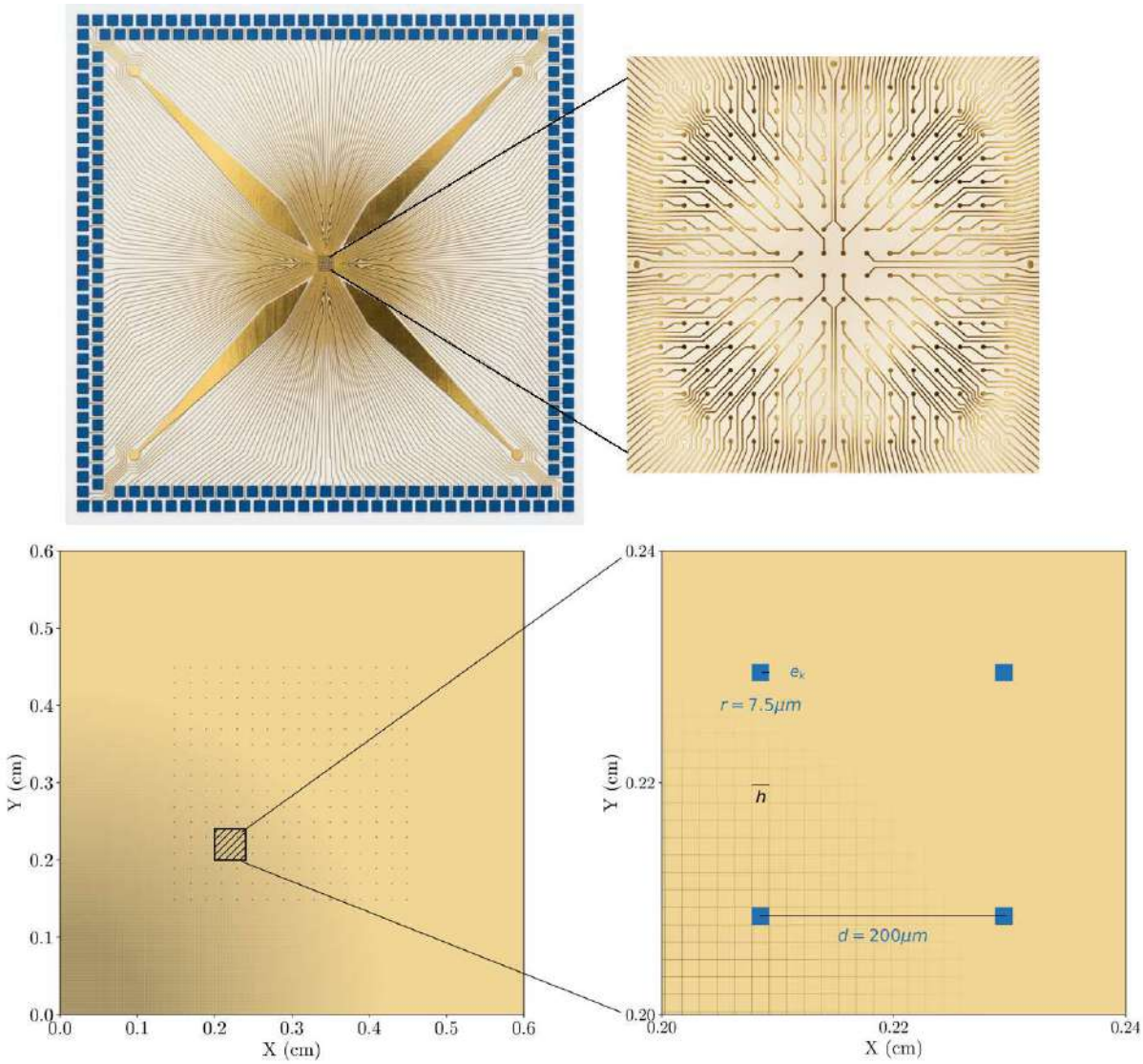

Figure 1: Schematic representation of the MEA experimental and computational domains. **Top**: layout of the MEA showing the full square electrode array as in the experimental setup. **Bottom**: on the left, computational domain with discretized electrode positions approximated as square surfaces, illustrating the correspondence between the physical and numerical representation. On the right, zoom on four electrodes, highlighting their physical dimensions and spatial arrangement within the domain. Post-processing of this image included color adjustments using a non-generative machine learning tool. No elements of the image were added, removed, or modified beyond visual enhancement.

Time integration was performed using a first-order Godunov operator splitting scheme [24], which decouples the different physical processes involved in the MEA model. Given a global time step Δt, each time interval $[t^n, t^{n+1}]$ is advanced through the following sequence:

(i) reaction step, in which the system of ordinary differential equations describing membrane ionic dynamics is solved independently at each spatial node using the Rush–Larsen scheme for gating variables and the explicit Euler method for ionic concentrations;

(ii) diffusion step, in which the equations governing spatial diffusion of the transmembrane potential v and the extracellular potential u_e are integrated in time using the explicit Euler method;

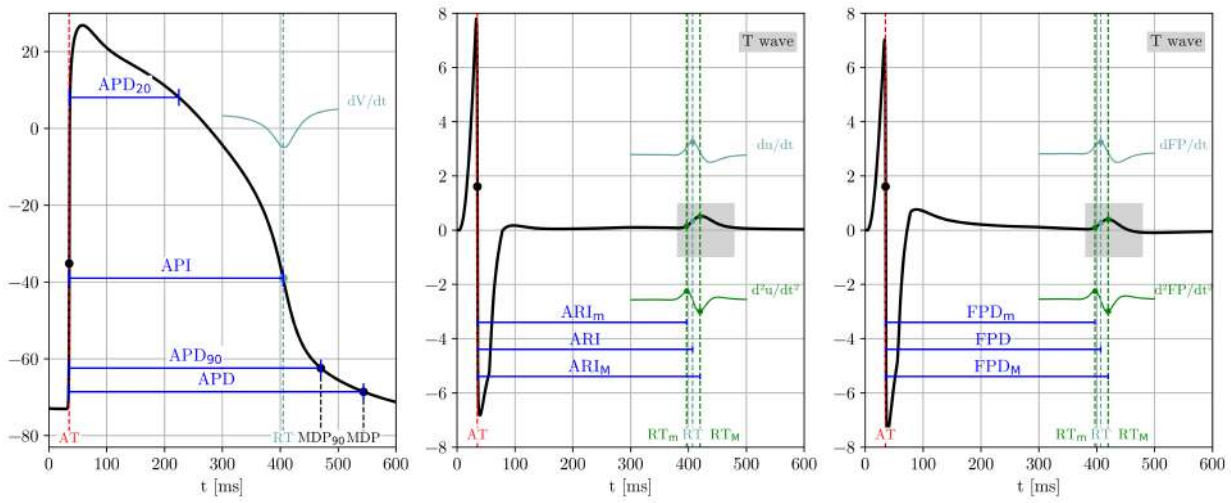

Figure 2: Illustration of duration-based biomarkers extracted from intracellular and extracellular signals. **Left panel**: AP (v). The first and second temporal derivatives are shown in the inset to highlight marker definitions. **Middle panel**: extracellular potential (u_e) and derivative zoom to clarify their identification. **Right panel**: FP with analogous markers and derivative inset illustrating the extraction procedure. This layout emphasizes the relationship between intracellular APs and extracellular signals.

(iii) electrode step, in which the ordinary differential equation describing electrode dynamics is solved for each electrode location as introduced in Eq. (5). The electrode current I^k is advanced using the explicit Euler scheme and the corresponding FP is computed as $U^k_{\mathrm{FP}} = R_i I^k$.

This first-order operator splitting ensures a stable and consistent coupling between cellular electrophysiology, extracellular field dynamics, and electrode behavior, while preserving an overall first-order accuracy in time.

All simulations were performed on the high-performance computing cluster of the University of Pavia (FAT nodes). Each simulation was executed on a single CPU node using shared-memory parallelization (32 cores, 256 GB RAM). The average wall-clock time required for a complete simulation was approximately 5.000 seconds.

Transmembrane, extracellular and FP biomarkers

Activation and repolarization biomarkers were extracted from three electrophysiological signals. At a spatial point $\boldsymbol{x} \in \Omega$, we denote

$$v_x(t) = v(\boldsymbol{x}, t), \qquad u_{e,x}(t) = u_e(\boldsymbol{x}, t), \qquad \mathrm{FP}_x(t) = \mathrm{FP}(\boldsymbol{x}, t). \tag{9}$$

For each signal, activation and recovery times were identified from characteristic morphological features of the corresponding waveform, as illustrated in Figure 2 and summarized in Table 2.

Biomarkers derived from the transmembrane AP were considered the reference timing of cellular depolarization and repolarization processes. In particular, the activation time $\mathrm{AT}_v(\boldsymbol{x})$ was defined as the instant of maximum upstroke velocity of $v_x(t)$, while repolarization times were identified either from the minimum of the temporal derivative during the downstroke or through threshold-based criteria, such as the membrane diastolic potential and the 90% repolarization level. These definitions allow the computation of the AP duration (APD and APD_{90}), providing a direct measure of cellular repolarization dynamics.

Extracellular and FP biomarkers were defined using analogous derivative-based criteria. Activation times for both $u_{e,x}(t)$ and $\mathrm{FP}_x(t)$ were identified from extrema of the first temporal derivative within the QRS complex, corresponding

Signal	Biomarker	Definition	Physiological meaning
AP	$\mathrm{AT}_v(\boldsymbol{x})$	$\underset{t\in\text{upstroke}}{\mathrm{argmax}}\partial_t v_x(t)$	Activation time, defined as the instant of maximum upstroke velocity of the AP.
AP	$\mathrm{RT}_v(\boldsymbol{x})$	$\underset{t\in\text{downstroke}}{\mathrm{argmin}}\ \partial_t v_x(t)$	Repolarization time, corresponding to the maximum downstroke velocity of the AP.
AP	$\mathrm{MDP}(\boldsymbol{x})$	–	Membrane diastolic potential, defined as the minimum value of the AP during the downstroke.
AP	$\mathrm{MDP}_{90}(\boldsymbol{x})$	–	Time instant at which the AP reaches 90% of its repolarization level.
AP	$\mathrm{APD}(\boldsymbol{x})$	$\mathrm{MDP}(\boldsymbol{x}) - \mathrm{AT}_v(\boldsymbol{x})$	AP duration.
AP	$\mathrm{APD}_{90}(\boldsymbol{x})$	$\mathrm{MDP}_{90}(\boldsymbol{x}) - \mathrm{AT}_v(\boldsymbol{x})$	AP duration at 90% repolarization.
AP	API	$\mathrm{RT}_v(\boldsymbol{x}) - \mathrm{AT}_v(\boldsymbol{x})$	AP interval.
u_e	$\mathrm{AT}_{ue}(\boldsymbol{x})$	$\underset{t\in\text{QRS}}{\mathrm{argmin}}\partial_t u_{e,x}(t)$	Extracellular activation time, associated with the depolarization wavefront.
u_e	$\mathrm{RT}_{ue}(\boldsymbol{x})$	$\underset{t\in\text{T wave}}{\mathrm{argmin}}\partial_t u_{e,x}(t)$	Extracellular repolarization time, associated with the T-wave extremum.
u_e	$\mathrm{RT}_{\mathrm{m}}(\boldsymbol{x})$	$\underset{t\in\text{T wave}}{\mathrm{argmin}}\partial_{tt} u_{e,x}(t)$	Instant corresponding to the first change of convexity of the extracellular signal during repolarization.
u_e	$\mathrm{RT}_{\mathrm{M}}(\boldsymbol{x})$	$\underset{t\in\text{T wave}}{\mathrm{argmax}}\partial_{tt} u_{e,x}(t)$	Instant corresponding to the second change of convexity of the extracellular signal during repolarization.
u_e	$\mathrm{ARI}(\boldsymbol{x})$	$\mathrm{RT}_{ue}(\boldsymbol{x}) - \mathrm{AT}_{ue}(\boldsymbol{x})$	Activation recovery interval (ARI).
u_e	$\mathrm{ARI}_{\mathrm{m}}(\boldsymbol{x})$	$\mathrm{RT}_{\mathrm{m}}(\boldsymbol{x}) - \mathrm{AT}_{ue}(\boldsymbol{x})$	Minimum activation recovery interval.
u_e	$\mathrm{ARI}_{\mathrm{M}}(\boldsymbol{x})$	$\mathrm{RT}_{\mathrm{M}}(\boldsymbol{x}) - \mathrm{AT}_{ue}(\boldsymbol{x})$	Maximum activation recovery interval.
FP	$\mathrm{AT}_{\mathrm{FP}}(\boldsymbol{x})$	$\underset{t\in\text{QRS}}{\mathrm{argmin}}\partial_t \mathrm{FP}_x(t)$	FP activation time.
FP	$\mathrm{RT}_{\mathrm{FP}}(\boldsymbol{x})$	$\underset{t\in\text{T wave}}{\mathrm{argmin}}\partial_t \mathrm{FP}_x(t)$	FP repolarization time.
FP	$\mathrm{RT}_{\mathrm{m}}(\boldsymbol{x})$	$\underset{t\in\text{T wave}}{\mathrm{argmin}}\partial_{tt} \mathrm{FP}_x(t)$	First change of convexity of the FP during repolarization.
FP	$\mathrm{RT}_{\mathrm{M}}(\boldsymbol{x})$	$\underset{t\in\text{T wave}}{\mathrm{argmax}}\partial_{tt} \mathrm{FP}_x(t)$	Second change of convexity of the FP during repolarization.
FP	$\mathrm{FPD}(\boldsymbol{x})$	$\mathrm{RT}_{\mathrm{FP}}(\boldsymbol{x}) - \mathrm{AT}_{\mathrm{FP}}(\boldsymbol{x})$	FP duration (FPD).
FP	$\mathrm{FPD}_{\mathrm{m}}(\boldsymbol{x})$	$\mathrm{RT}_{\mathrm{m}}(\boldsymbol{x}) - \mathrm{AT}_{\mathrm{FP}}(\boldsymbol{x})$	Minimum FP duration.
FP	$\mathrm{FPD}_{\mathrm{M}}(\boldsymbol{x})$	$\mathrm{RT}_{\mathrm{M}}(\boldsymbol{x}) - \mathrm{AT}_{\mathrm{FP}}(\boldsymbol{x})$	Maximum FP duration.

Table 1: Definition of the electrophysiological biomarkers extracted from the intracellular AP, extracellular potential (u_e), and FP. The table reports the mathematical formulation used to identify activation and repolarization instants from the temporal derivatives of each signal, together with the corresponding physiological interpretation. Duration-based metrics such as APD, ARI, and FPD are computed as time intervals between the corresponding activation and repolarization markers.

to the passage of the depolarization wavefront beneath the recording location. Repolarization times were extracted from the T-wave morphology by locating extrema of the first derivative, while additional repolarization markers were identified by detecting changes in signal convexity through the second temporal derivative.

These definitions enable the computation of activation–recovery intervals (ARI) from extracellular signals and FPD from MEA recordings.

Finally, ad additional biomarker was considered. We analyze the biomarker $\mathrm{APD}_{20/90}$, which is defined as the ratio between the APD measured at 20% and 90% repolarization levels and provides a quantitative descriptor of the plateau phase and triangulation of the AP.

For each simulation, the waveforms $v_x(t)$ and $u_{e,x}(t)$ were stored at 900 uniformly distributed locations across the computational domain. Biomarkers were subsequently extracted in a post-processing step according to the definitions

reported in Table 2. Transmembrane biomarkers were used as reference values for the quantitative correlation analysis presented in the Results section.

For duration-related biomarkers (APD, ARI, and FPD), quantitative comparisons were performed by analyzing their relationships under increasing levels of tissue heterogeneity. For each configuration, vectors of paired biomarkers were constructed and a linear regression analysis was carried out. The regression line and the corresponding coefficient of determination R^2 were computed, where R^2 quantifies the proportion of variance explained by the linear model and provides a measure of the strength of the association between biomarkers.

For intracellular and extracellular signals, the analysis was conducted on vectors of length $n = 900$ corresponding to uniformly sampled tissue points, focusing on the relationship between APD and ARI-based biomarkers extracted from u_e. For MEA recordings, vectors of length $n = 256$ were constructed at electrode locations, and the correlation analysis was performed between APD and FP-based duration biomarkers.

In order to validate the robustness of the results, correlation analyses were performed also in altered configurations. In particular, we consider 4-Aminopyridine (4-AP), a potassium channel blocker that primarily inhibits the ultra-rapid delayed rectifier current (I_{Kur}), which is predominantly expressed in AL cardiomyocytes. As a consequence, its electrophysiological effect is expected to be minimal in purely VL tissues, while selectively prolonging APD in AL cells, as depicted in the Supplementary Material, Figure S3. The effect of 4-AP was simulated as an 80% reduction of the I_{Kur} maximum conductance, corresponding to a pharmacological block induced by a concentration of $50\,\mu\mathrm{M}$, consistently with dose-response data reported for human cardiomyocytes [4, 29, 30]. Human adult cardiomyocytes are used as a reference since quantitative information on I_{Kur} density in isolated hiPSC-CMs is currently limited, as the genes encoding for I_{Kur} channel subunits are absent in the early phases of cardiac embryogenesis and are progressively expressed during heart development.

Results

Electrophysiological heterogeneity is an intrinsic feature of hiPSC-derived cardiac tissues and represents one of the main sources of variability observed in MEA experiments. This heterogeneity arises from several factors, including differences among cell lines, variability in differentiation protocols, and incomplete maturation of the derived cardiomyocytes. As a result, hiPSC-CM preparations typically exhibit mixed populations of cells displaying VL and AL electrophysiological phenotypes.

Effect of tissue heterogeneity on propagation and signal morphology

Figure 3 illustrates the impact of increasing AL cell content on propagation dynamics, waveform morphology, and electrophysiological signals. Four configurations are considered, ranging from a homogeneous VL tissue to progressively heterogeneous tissues containing 10%, 20%, and 30% AL hiPSC-CMs randomly distributed within the domain. At the cellular level, increasing heterogeneity induces clear modifications in AP morphology. In particular, the APD progressively decreases and the repolarization phase becomes faster, resulting in a more triangular AP profile. This behavior reflects the contribution of AL ionic dynamics and leads to an overall reduction of APD across the tissue. Consistently, APD_{90} decreases from $411.63\,\mathrm{ms}$ in the homogeneous VL configuration to $390.3\,\mathrm{ms}$ in the 30% heterogeneous configuration, without evidence of a marked increase in spatial standard deviation.

These cellular-level changes are also reflected in the extracellular and FP signals. In the extracellular potential u_e, the amplitude of the T wave progressively decreases as heterogeneity increases. Concurrently, the temporal separation between depolarization and repolarization phases is also reduced, consistently with the shortening of APD observed at the cellular level. This effect is even more pronounced in the FP recordings, where repolarization-related components become progressively less distinguishable. In particular, while depolarization features of the FP signals remain

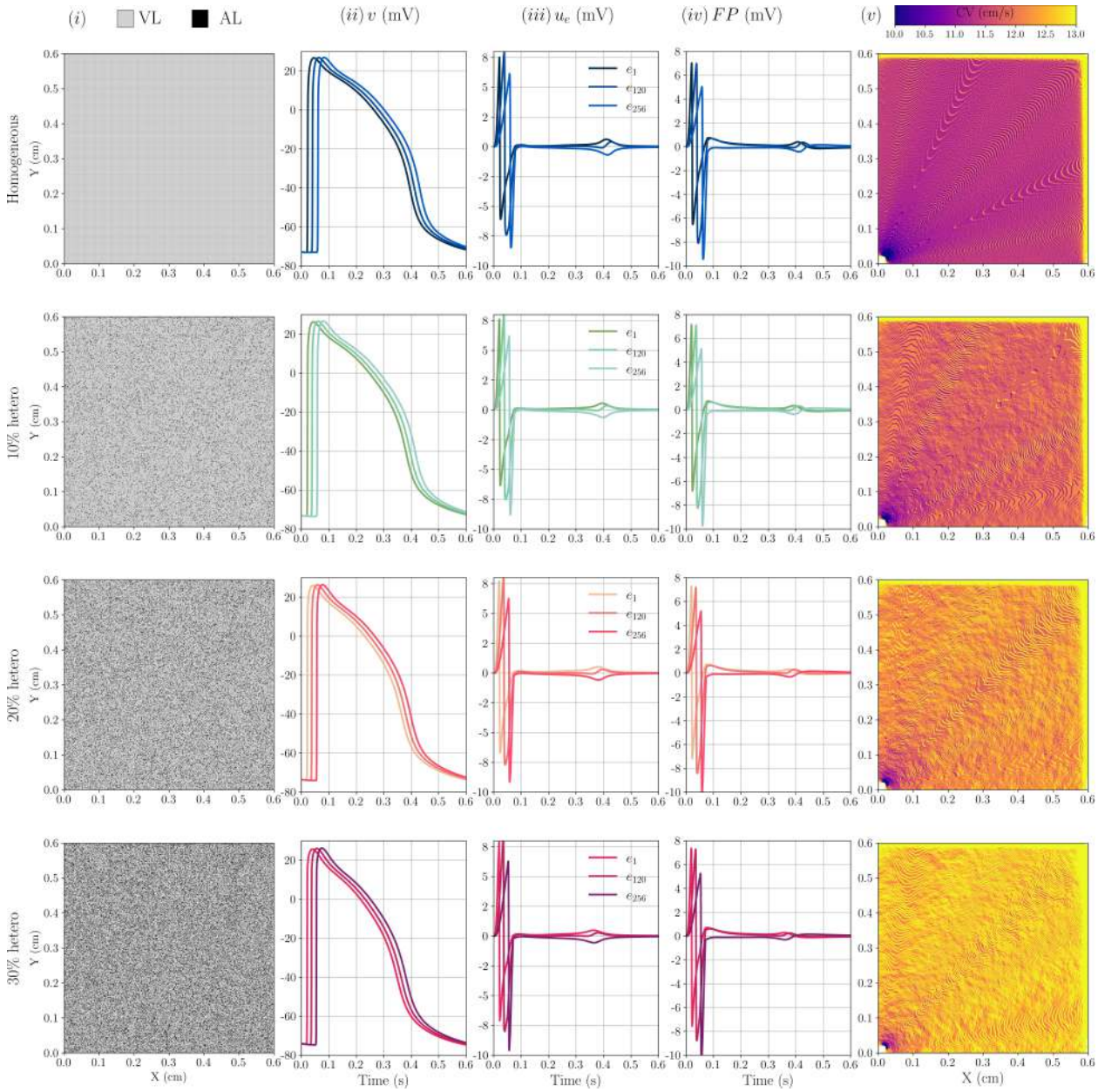

Figure 3: Effect of tissue heterogeneity on propagation and signal morphology. Rows correspond to increasing fractions of AL cells randomly distributed within VL tissue, from 0% to 30%. Columns report: *(i)* spatial distribution of AL and VL phenotypes in the 2D domain; *(ii)* intracellular APs recorded at three locations along the main diagonal; *(iii)* extracellular potentials (u_e) at the same positions; *(iv)* FPs recorded by three electrodes aligned along the diagonal (first, central, and last electrode); and *(v)* pointwise CV maps. The figure illustrates the progressive changes in propagation speed and signal morphology induced by increasing phenotypic heterogeneity.

clearly identifiable, the T-wave morphology becomes significantly attenuated and less well defined compared to the corresponding extracellular signals.

Moreover, as the degree of heterogeneity increases, a consistent increase in conduction velocity (CV) is observed, as reflected by the CV maps, where higher values of the CV are coloured in yellow in the last column of Figure 3. The presence of AL cells, characterized by faster intrinsic ionic dynamics, leads to a global acceleration of electrical propagation despite their random spatial distribution. Coherently, activation times become closer as propagation speed

VL (%)	AP biomarker (X)	corr(X,$\mathrm{ARI_m}$)	corr(X,$\mathrm{ARI_M}$)	corr(X,$\mathrm{FPD_m}$)	corr(X,$\mathrm{FPD_M}$)
100	APD	0.9921	0.9831	0.8765	0.7298
	$\mathrm{APD_{90}}$	0.9918	0.9821	0.8744	0.7346
	$\mathrm{APD_{20/90}}$	0.9791	0.9631	0.8013	0.6141
90	APD	0.9544	0.9329	0.8658	0.7121
	$\mathrm{APD_{90}}$	0.9621	0.9426	0.8655	0.7180
	$\mathrm{APD_{20/90}}$	0.9441	0.9403	0.4044	0.2977
80	APD	0.8715	0.8778	0.8374	0.6815
	$\mathrm{APD_{90}}$	0.8859	0.8920	0.8335	0.6839
	$\mathrm{APD_{20/90}}$	0.8211	0.8176	0.4531	0.3158
70	APD	0.8623	0.8971	0.7234	0.5472
	$\mathrm{APD_{90}}$	0.8737	0.9073	0.7235	0.5526
	$\mathrm{APD_{20/90}}$	0.6270	0.6720	0.4749	0.3300
70% + 4-AP	APD	0.9098	0.9209	0.7117	0.5138
	$\mathrm{APD_{90}}$	0.9110	0.9223	0.7072	0.5150
	$\mathrm{APD_{20/90}}$	0.7977	0.7992	0.5177	0.3538

Table 2: Pearson correlation coefficients between duration-based biomarkers extracted from intracellular APs and the corresponding extracellular markers derived from u_e ($\mathrm{ARI_m}$, $\mathrm{ARI_M}$) and FPs ($\mathrm{FPD_m}$, $\mathrm{FPD_M}$). The first column reports the percentage of VL cells in the tissue, corresponding to increasing levels of phenotypic heterogeneity. AP-based biomarkers (APD, $\mathrm{APD_{90}}$, and $\mathrm{APD_{20/90}}$) are used as reference quantities and correlated with their extracellular counterparts. The last block reports the case with 70% VL cells under 4-AP treatment.

increases. Quantitatively, the global activation spread, defined as $\Delta\,\mathrm{AT}_v = \mathrm{AT}_v^{\max} - \mathrm{AT}_v^{\min}$ between the earliest and latest activated cells (located at diagonally opposite points of the domain), decreases from $12.15\,\mathrm{ms}$ in the homogeneous VL tissue to $11.01\,\mathrm{ms}$ in the 30% heterogeneous configuration.

Overall, these results show that increasing tissue heterogeneity affects not only propagation speed and AP morphology, but also the morphology of extracellular and FP waveforms within the present *in-silico* framework. In particular, the progressive attenuation of repolarization features in FP signals should be interpreted as a model-based observation: in our simulations, conductivity parameters (σ_i, σ_e) and other tissue/electrode parameters are kept fixed across configurations, so the observed changes primarily arise from phenotypic mixing and spatial averaging in the computed signals. Therefore, the greater sensitivity of FP-based duration biomarkers compared with extracellular biomarkers is a numerical-mechanistic result of this controlled setup.

Biomarker correlation analysis

The relationship between duration-based biomarkers was assessed through linear regression analyses between AP-derived and extracellular- or FP-derived markers. The results are illustrated in Figure 4: the upper panels report the analysis performed on the 900 sampled tissue points (u_e vs AP), while the lower panels show the corresponding analysis at the 256 MEA electrode locations (FP vs AP). Biomarkers based on API and FPD were not included in the main analysis. API exhibits reduced sensitivity to repolarization dynamics and does not capture the variability reflected in extracellular signals. Conversely, FPD-based biomarkers are derived from extrema of the first temporal derivative and are therefore more sensitive to numerical discretization, leading to clustering effects and biased correlations. For completeness, these analyses are reported in the Supplementary Material, Figure S1 and Figure S2.

In the homogeneous configuration (100% VL), extracellular biomarkers exhibited a very strong linear correlation with intracellular references. In particular, both $\mathrm{FPD_m}$ and $\mathrm{FPD_M}$ showed excellent agreement with APD and $\mathrm{APD_{90}}$, with coefficients of determination consistently above 0.98 for u_e-based biomarkers. This result indicates that, in the absence of phenotypic heterogeneity, extracellular duration markers accurately reflect intracellular repolarization dynamics at the tissue level.

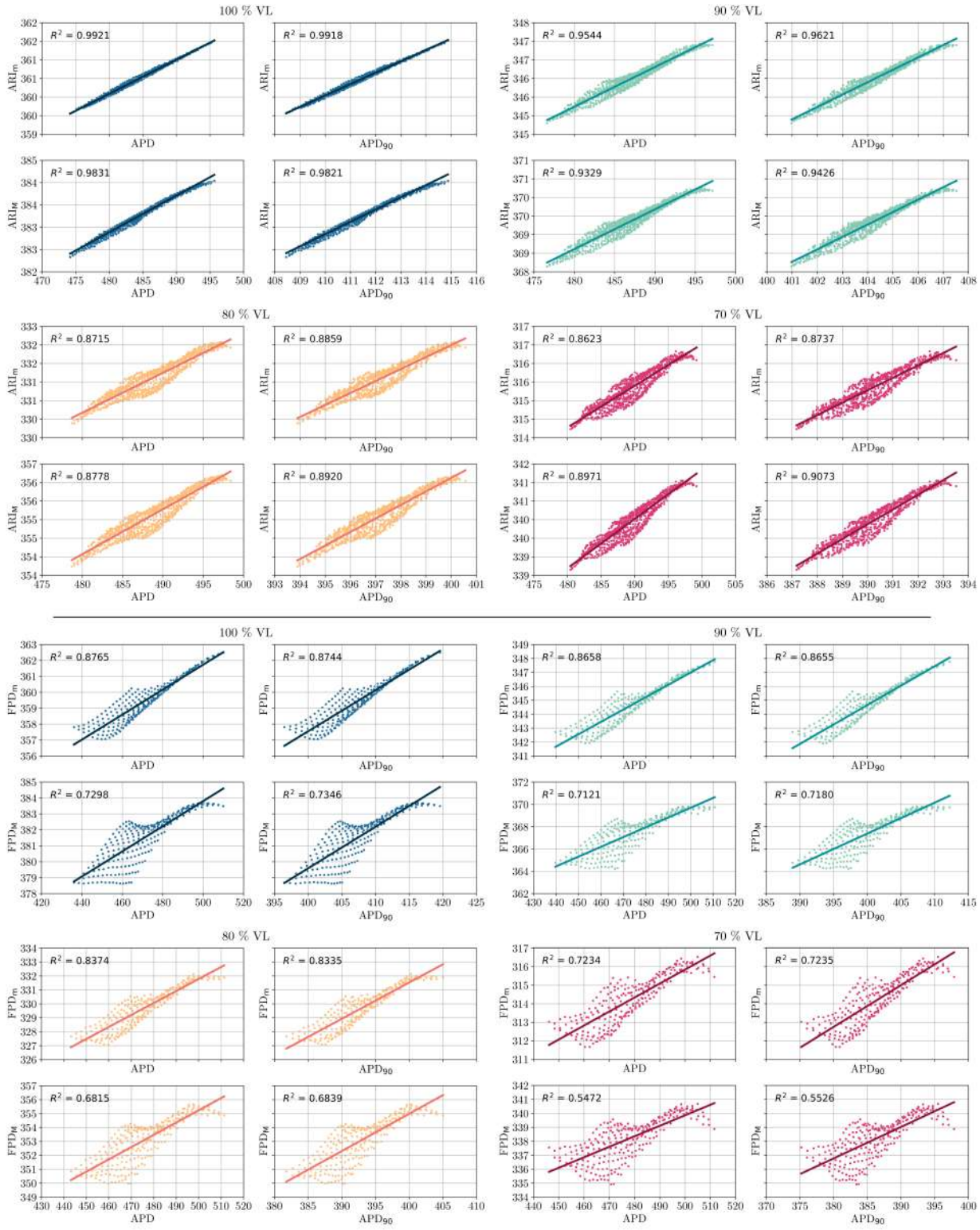

Figure 4: Linear regression analysis between AP-derived and extracellular or FP-derived duration biomarkers. **Upper panels**: scatter plots and regression lines for the 900 sampled tissue points. **Lower panels**: corresponding analysis at the 256 MEA electrode locations, comparing the same AP-based biomarkers with FP-derived duration markers.

In contrast, FP-derived biomarkers displayed systematically lower correlations with AP-based durations already in the homogeneous case. While $\mathrm{FPD_M}$ maintained a relatively high correlation (up to $R^2 \approx 0.88$), $\mathrm{FPD_M}$ showed a more pronounced reduction ($R^2 \approx 0.73$). This difference is consistent with the spatial averaging inherent to FP recordings, as each electrode integrates signals originating from multiple cells within its sensing area.

For extracellular signals sampled at 900 tissue locations, the correlation between $\mathrm{FPD_M}$ and APD/$\mathrm{APD_{90}}$ remained high down to the 80% VL configuration, while a noticeable reduction emerged in the 70% VL case, particularly for $\mathrm{FPD_M}$. Nevertheless, u_e-based biomarkers consistently preserved a strong association with intracellular durations, with R^2 values remaining above 0.86 in all configurations considered (see Table 2).

Conversely, FP-based biomarkers exhibited a stronger sensitivity to increasing heterogeneity. Both $\mathrm{FPD_m}$ and $\mathrm{FPD_M}$ showed a monotonic decrease in R^2 as the percentage of AL cells increased, with the effect being substantially stronger for $\mathrm{FPD_M}$. In the 70% VL configuration, correlations between FP-derived and AP-based durations dropped to moderate levels ($R^2 \approx 0.55$ for $\mathrm{FPD_M}$), indicating that FP biomarkers increasingly reflect the mixed phenotypic composition beneath each electrode rather than a direct intracellular reference.

Overall, these results show that extracellular biomarkers computed at the tissue level provide a robust surrogate of intracellular repolarization dynamics even in heterogeneous settings, whereas FP-derived duration markers are more affected by phenotypic mixing and spatial averaging. This effect becomes increasingly relevant as tissue heterogeneity grows and should be considered when interpreting MEA-based biomarkers in mixed hiPSC-CM preparations.

Validation through $\mathrm{APD}_{20/90}$

$\mathrm{APD}_{20/90}$ has been shown to be particularly effective in discriminating AL and VL hiPSC-derived cardiomyocytes, as it captures differences in early repolarization dynamics that are not fully reflected by standard APD or APD_{90} metrics.

As depicted in Figure 5, in homogeneous tissue configurations, $\mathrm{APD}_{20/90}$ extracted from intracellular APs remains strongly correlated with extracellular repolarization markers derived from u_e. This behavior is consistent with the fact that, at the cellular level, $\mathrm{APD}_{20/90}$ reliably encodes the underlying electrophysiological phenotype. High correlation values reported in Table 2 for low heterogeneity levels confirm the validity of $\mathrm{APD}_{20/90}$ as a reference biomarker in controlled conditions.

Overall, this analysis highlights a fundamental limitation of FP-based repolarization biomarkers in heterogeneous tissues while reinforcing the role of $\mathrm{APD}_{20/90}$ as a discriminative intracellular reference. At the same time, it provides insight into which extracellular descriptors remain more robust when transitioning from single-cell to tissue-level measurements.

Validation through 4-AP perfusion

To further investigate the robustness and physiological interpretability of duration-based biomarkers under pharmacological perturbation, we analyze the effect of 4-AP by directly comparing heterogeneous tissues with a homogeneous VL reference configuration, see Figure 6.

The phenotype selectivity of 4-AP is clearly confirmed by our simulations: in the heterogeneous configuration, APD_{90} increases from approximately $390\,\mathrm{ms}$ (untreated) to approximately $405\,\mathrm{ms}$ after 4-AP, moving much closer to the homogeneous VL reference value of about $411\,\mathrm{ms}$.

A markedly different behavior is observed in the heterogeneous configuration (70% VL + 4-AP). In this case, the presence of AL cells leads to a selective prolongation of the repolarization phase at the intracellular level, while CV and activation patterns remain essentially unchanged with respect to the not-treated condition. When compared to the homogeneous VL case, the correlation structure is significantly altered: although correlations remain high, they are

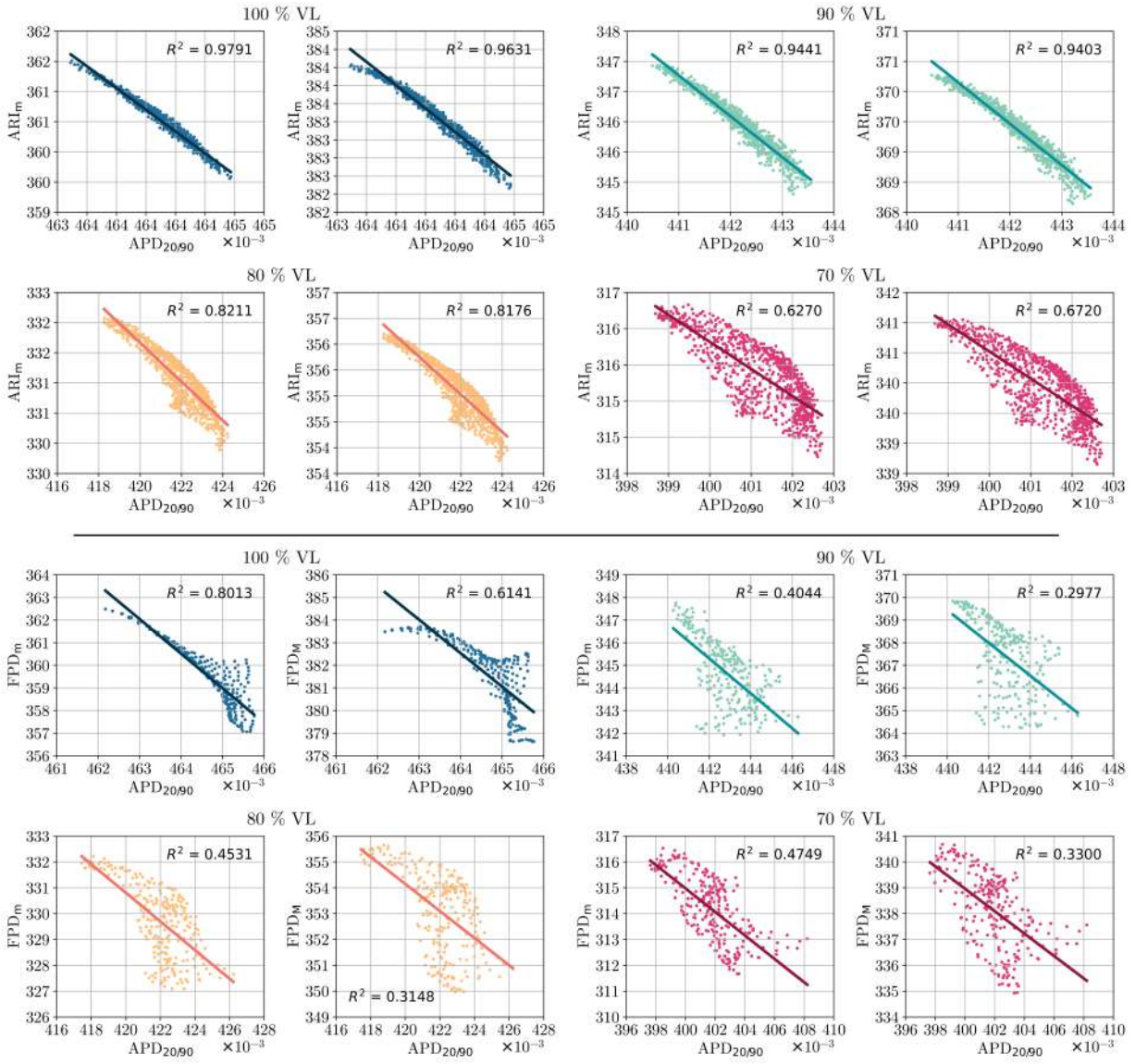

Figure 5: Linear regression analysis between $APD_{20/90}$ and extracellular or FP-derived duration biomarkers. **Upper panels**: scatter plots and regression lines for the 900 sampled tissue points. **Lower panels**: corresponding analysis at the 256 MEA electrode locations, comparing $APD_{20/90}$ with FP-derived duration markers (FPD_m and FPD_M).

systematically lower than in the 100% VL configuration (e.g., $\mathrm{corr}(\mathrm{APD}, \mathrm{ARI_m}) = 0.8623$ vs 0.9921), reflecting the increased electrophysiological heterogeneity induced by the drug acting only on a subpopulation of cells.

This comparison highlights that the effect of 4-AP is not global but spatially localized, being confined to AL cells. As a result, extracellular signals and especially FP recordings integrate responses from both affected and unaffected cells, leading to a partial loss of correlation with intracellular biomarkers (see Figure 7). This effect is particularly evident for FP-based descriptors, whose correlations remain substantially lower than those observed in the homogeneous VL case.

Overall, the direct comparison with the homogeneous VL configuration demonstrates that 4-AP preserves physiological specificity by selectively targeting AL cells, while simultaneously amplifying the impact of tissue heterogeneity on extracellular biomarkers. This provides a stringent validation scenario, showing that intracellular markers fully capture drug-induced effects, whereas FP-based measurements only partially reflect them in mixed-cell populations.

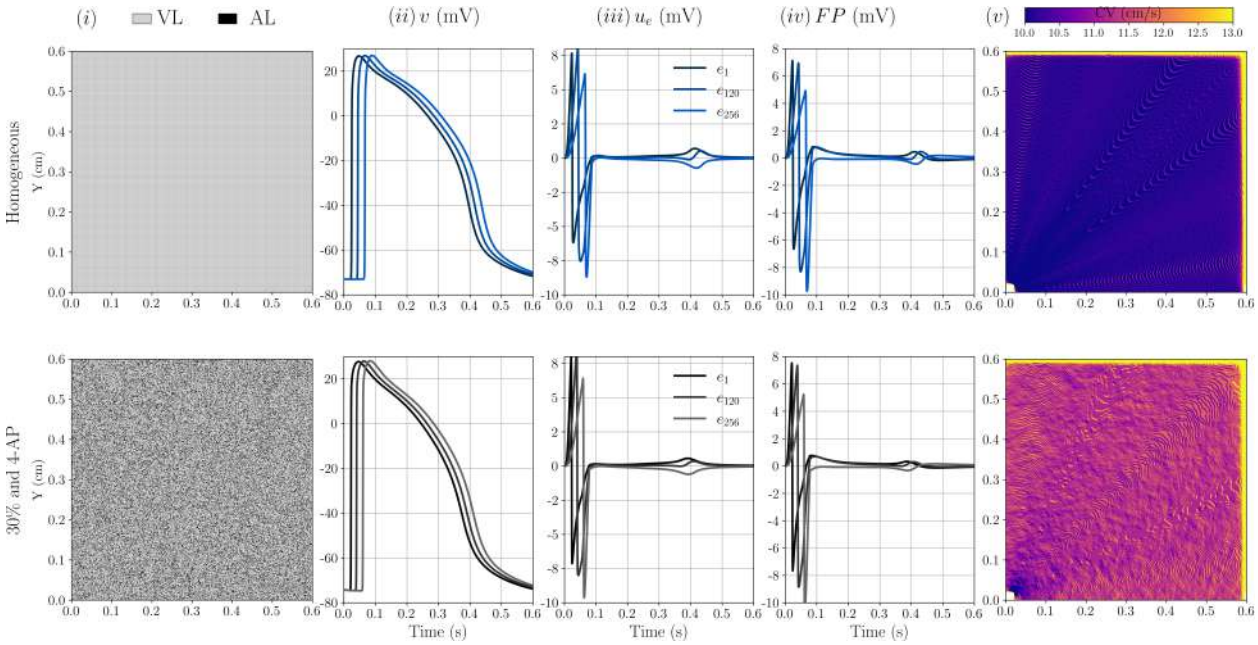

Figure 6: Effect of 4-AP on heterogeneous tissues. The layout of the figure is the same as in Fig. 3. The two rows correspond to homogeneous VL tissues and heterogeneous tissues with 30% AL cells randomly distributed within VL tissue, perfused with 4-AP. Columns report the spatial phenotype distribution, intracellular APs recorded at three locations along the main diagonal, extracellular potentials (u_e) at the same positions, FPs recorded by three electrodes aligned along the diagonal, and the corresponding pointwise CV maps. The comparison highlights the electrophysiological changes induced by retinoic acid in heterogeneous tissues.

Discussion

In this study, we investigated how tissue heterogeneity and electrode-level spatial averaging influence the relationship between intracellular electrophysiological dynamics and extracellular or MEA-derived biomarkers in heterogeneous tissues composed of AL and VL hiPSC-derived cardiomyocytes. Using a multiscale computational framework integrating cellular electrophysiology, tissue-level propagation, and explicit MEA signal reconstruction, we systematically assessed how phenotypic heterogeneity and pharmacological perturbations affect the reliability of commonly used duration-based biomarkers. Our results show that extracellular repolarization markers derived from the pointwise extracellular potential maintain strong correlations with intracellular AP dynamics, including APD and APD_{90}, even in the presence of substantial AL cell fractions. In contrast, FP-derived biomarkers progressively lose specificity as tissue heterogeneity increases. This behavior reflects the intrinsic spatial averaging of MEA recordings, where each electrode integrates signals generated by multiple neighboring cells with distinct electrophysiological properties. Consequently, FP waveforms represent a composite electrophysiological response rather than the activity of individual cardiomyocytes, similarly to how ECGs emerge from spatially distributed cardiac sources. This mechanism provides a plausible explanation for the variability frequently observed in MEA-based hiPSC-CM assays and demonstrates that extracellular signals sampled directly at the tissue level remain more reliable surrogates of intracellular repolarization dynamics when sufficiently dense spatial sampling is available. Previous computational studies investigated the relationship between intracellular electrophysiology and extracellular MEA recordings in hiPSC-CM preparations, mainly focusing on FP generation and drug-induced electrophysiological responses [1, 27]. However, the quantitative impact of tissue heterogeneity and electrode spatial averaging on the correspondence between intracellular AP biomarkers and extracellular or FP-derived descriptors remains insufficiently characterized. This has important implications for the interpretation of MEA-based assays in the context of preclinical drug screening. For instance, in the context of preclinical cardiac safety assessment and the Comprehensive *in-vitro* Proarrhythmia Assay (CiPA) initiative, an interna-

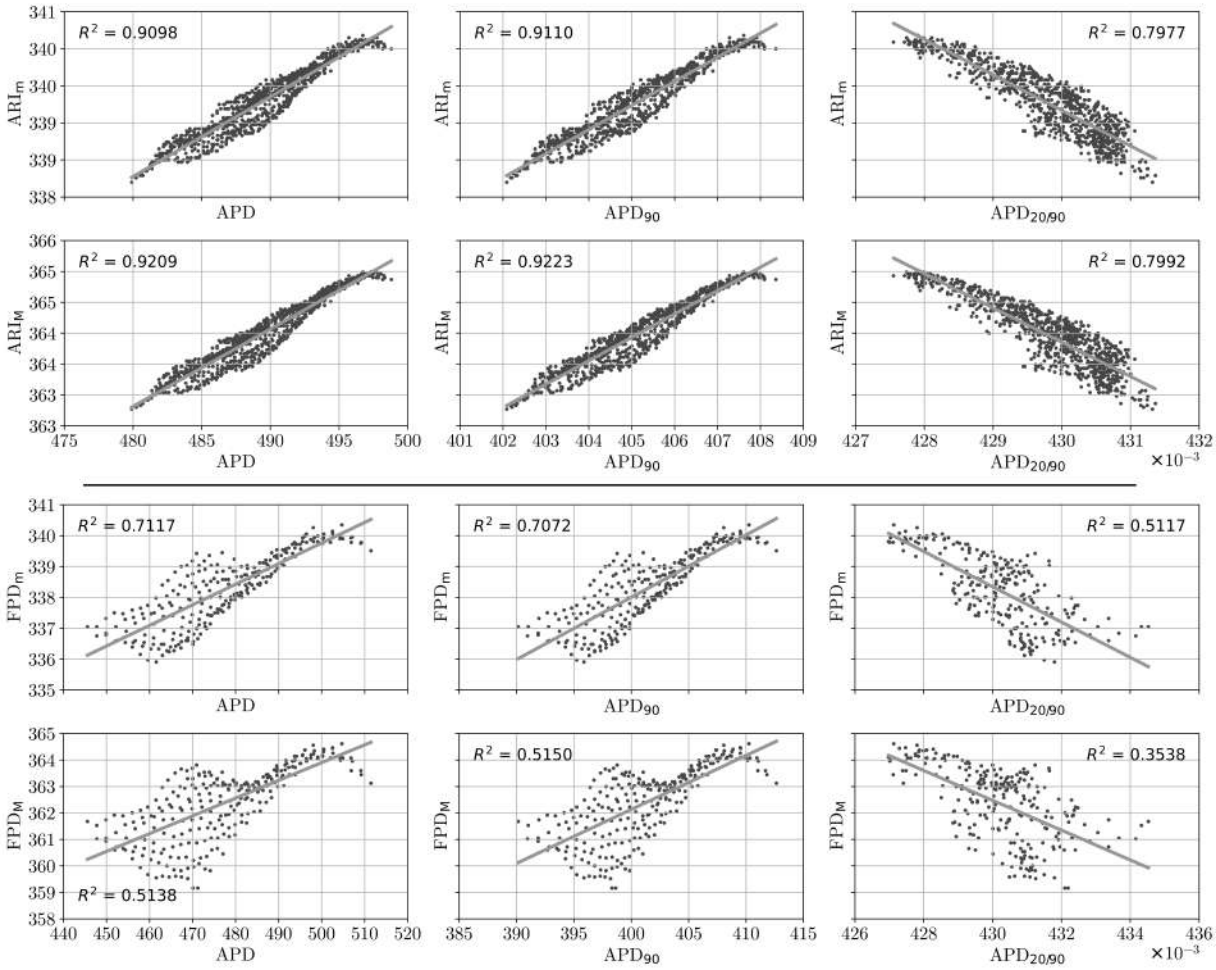

Figure 7: Linear regression analysis between AP-derived and extracellular or FP-derived duration biomarkers under 4-AP perfusion. **Upper panels**: scatter plots and regression lines for the 900 sampled tissue points. **Lower panels**: corresponding analysis at the 256 MEA electrode locations, comparing the same AP-based biomarkers with FP-derived duration markers.

tional framework developed to improve prediction of drug-induced proarrhythmic risk using integrated ion-channel testing, in-silico modeling, and hiPSC-CM electrophysiology assays, FP duration is commonly used as a surrogate of QT/AP prolongation in hiPSC-CMs [8, 31]. Our simulations indicate that the reliability of FP-derived biomarkers strongly depends on tissue composition and maturation state, suggesting that part of the variability observed across MEA platforms may arise not only from technical factors, but also from intrinsic biological heterogeneity within the cardiac preparation.

A key finding of this work is that biomarkers associated with early repolarization dynamics, such as $\mathrm{ARI_m}$ and $\mathrm{FPD_m}$, consistently outperform maximum-based descriptors under increasing heterogeneity and pharmacological perturbation. Early repolarization remains more temporally closer to the depolarization wavefront, whereas late repolarization emerges from spatially distributed recovery processes that are more susceptible to desynchronization and averaging effects.

The introduction of $\mathrm{APD}_{20/90}$ further highlights the importance of capturing detailed repolarization dynamics when characterizing mixed hiPSC-CM tissues. This biomarker has previously been proposed as an effective discriminator between AL and VL phenotypes at the cellular level, as it reflects differences in plateau morphology and AP triangulation

[2, 6]. Our analysis confirms that $\mathrm{APD}_{20/90}$ retains strong correlations with extracellular repolarization markers in relatively homogeneous conditions, but becomes increasingly difficult to recover from FP recordings as tissue heterogeneity grows. This result emphasizes the limitations of electrode-based measurements in resolving subtle repolarization features that originate at the cellular scale. From a physiological perspective, $\mathrm{APD}_{20/90}$ is especially relevant because atrial and ventricular phenotypes are characterized by distinct repolarization profiles: AL cells typically exhibit a shorter and less pronounced plateau phase, whereas VL cells show a longer and more structured repolarization. As a result, $\mathrm{APD}_{20/90}$ has emerged as a robust cellular-level biomarker for subtype classification and maturation assessment in both experimental and *in-silico* studies. However, as tissue heterogeneity increases, a progressive degradation of correlation is observed, particularly when FP-based biomarkers are considered. This effect can be attributed to the spatial averaging intrinsic to MEA recordings: while $\mathrm{APD}_{20/90}$ is well defined at the cellular level and allows a clear discrimination between AL and VL cells, extracellular signals recorded by a single electrode reflect the superposition of contributions from multiple cells with potentially different phenotypes. In highly heterogeneous configurations, this mixing effect reduces the ability of FP-derived markers to resolve repolarization features associated with $\mathrm{APD}_{20/90}$. Interestingly, correlations involving minimum-based biomarkers $\mathrm{ARI}_{\mathrm{m}}$ and $\mathrm{FPD}_{\mathrm{M}}$ systematically outperform those based on maximum values. This observation suggests that early repolarization events, which are more closely linked to local cellular dynamics, are less affected by spatial averaging than late repolarization features. Consequently, minimum-based markers maintain a stronger relationship with intracellular $\mathrm{APD}_{20/90}$ even in the presence of increasing heterogeneity. These observations may also help explain why immature hiPSC-CM preparations often exhibit substantial variability in FP morphology and repolarization metrics across laboratories and differentiation protocols. Immature cardiomyocytes display altered ionic expression profiles, reduced I_{K1} density, which contribute to heterogeneous electrophysiological behavior at the tissue level. In this context, the progressive degradation of FP-based biomarkers observed in our simulations suggests that tissue maturation and phenotypic purity are critical determinants for improving the interpretability and reproducibility of MEA assays. The pharmacological perturbation experiments performed using 4-Aminopyridine further support these conclusions. By selectively inhibiting I_{Kur}, 4-AP prolongs atrial repolarization without substantially affecting VL cells or propagation properties [12]. In heterogeneous tissues, this selective modulation amplifies electrophysiological differences between cell types. While intracellular and extracellular biomarkers are able to capture these changes with high fidelity, FP-derived descriptors show a reduced sensitivity due to the simultaneous integration of signals from both AL and VL regions.

Taken together, these results provide important insights into the interpretation of MEA-based electrophysiological biomarkers in hiPSC-CM preparations. In particular, our findings highlight that spatial averaging and phenotypic mixing can significantly affect the relationship between FP-derived markers and the underlying cellular electrophysiology. From a practical perspective, this suggests that biomarkers based on early repolarization features may represent more reliable indicators when translating single-cell electrophysiological information to tissue-level MEA recordings.

More broadly, the computational framework presented in this work offers a powerful tool for bridging cellular electrophysiology and experimental MEA measurements. By explicitly linking ionic dynamics, tissue heterogeneity, and electrode-level signals, such models can help interpret complex experimental datasets and guide the design of more robust electrophysiological biomarkers. Future work will extend this approach to larger tissue domains, additional pharmacological interventions, and more complex patterns of structural and electrophysiological heterogeneity, further improving the integration between computational modeling and experimental cardiac electrophysiology.

Conclusion

In this work we investigated the relationship between intracellular electrophysiological dynamics and extracellular biomarkers in heterogeneous tissues composed of AL and VL hiPSC-derived cardiomyocytes. Using a multiscale computational framework linking ionic models, tissue-level propagation, and MEA-scale signal reconstruction, we

systematically evaluated the reliability of duration-based biomarkers under increasing levels of phenotypic heterogeneity and pharmacological perturbation.

Our results show that extracellular repolarization markers derived from the extracellular potential u_e maintain a strong and consistent relationship with intracellular APDs across heterogeneous configurations. In contrast, biomarkers extracted from FP signals recorded at MEA electrodes are more strongly affected by spatial averaging and phenotypic mixing, leading to a progressive degradation of correlation with intracellular electrophysiological descriptors as tissue heterogeneity increases.

Across all analyzed conditions, biomarkers based on early repolarization events consistently exhibit greater robustness than those derived from late repolarization features. In particular, minimum-based descriptors maintain a stronger correspondence with intracellular dynamics even in heterogeneous and pharmacologically perturbed tissues. These findings suggest that early repolarization markers provide more reliable indicators when bridging single-cell electrophysiology and MEA-scale measurements.

Overall, this study provides a quantitative framework for interpreting extracellular and MEA-based biomarkers in mixed hiPSC-CM preparations. By clarifying the effects of spatial averaging, phenotypic heterogeneity, and selective pharmacological modulation, our results contribute to a more reliable interpretation of MEA recordings and support the development of more robust electrophysiological biomarkers for *in-vitro* cardiac models.

Supporting information

Figure S1 Correlation between FPD and intracellular biomarkers. Correlation analysis between FPD and intracellular biomarkers (API, APD, APD_{90}) for increasing levels of tissue heterogeneity. Scatter plots show vertical clustering of data points, highlighting numerical limitations associated with derivative-based FPD estimation.

Figure S2 Correlation between API and FPD-based biomarkers. Correlation analysis between API and FPD-derived biomarkers (FPD, $\mathrm{FPD}_{\mathrm{m}}$, $\mathrm{FPD}_{\mathrm{M}}$). The vertical alignment of data points reflects the reduced variability of API and its limited sensitivity to repolarization dynamics compared to extracellular markers.

Figure S3 Heterogeneity effect of 4-AP. Comparison between homogeneous VL tissue and heterogeneous configurations (30% AL) without and with 4-AP treatment. The figure reports phenotype distribution, intracellular APs, extracellular potentials (u_e), FP signals, and CV maps. The results highlight a selective prolongation of repolarization in AL regions after 4-AP exposure, while activation patterns and CV remain largely unchanged.

Acknowledgments

This work was supported by grants to L.B. from the Gustav & Ruth Jacob Foundation and Cecilia Augusta Foundation, and by grant to S.B. from the Swiss National Science Foundation, SNSF grants 217025.

Author Contributions Statement

S.B. and L.B. conceived the study. S.B. and M.F. developed the methodology and software. S.B. and C.A. performed the investigation, simulations, and data analysis. R.K. and L.B. supervised the research activity. S.B. wrote the main manuscript text. M.F. contributed to the computational implementation and manuscript preparation. C.A. contributed to manuscript writing and revision. R.K. and L.B. revised the manuscript and provided scientific input. All authors discussed the results and reviewed and approved the final manuscript.

References

[1] Emanuela Abbate, Muriel Boulakia, Yves Coudière, Jean-Frédéric Gerbeau, Philippe Zitoun, and Nejib Zemzemi. In silico assessment of the effects of various compounds in MEA/hiPSC-CM assays: Modeling and numerical simulations. *Journal of Pharmacological and Toxicological Methods*, 89:59–72, 2018. ISSN 1056-8719. https://doi.org/10.1016/j.vascn.2017.10.005.

[2] C. Altomare, C. Bartolucci, L. Sala, C. Balbi, J. Burrello, N. Pietrogiovanna, A. Burrello, S. Bolis, S. Pannella, M. Arici, R. Krause, M. Rocchetti, S. Severi, and L. Barile. A dynamic clamping approach using *in silico* IK1 current for discrimination of chamber-specific hiPSC-derived cardiomyocytes. *Communications Biology*, 6(1), 2023. 10.1038/s42003-023-04674-9.

[3] S. Botti, R. Krause, and L.F. Pavarino. In-silico modeling of multi-electrode arrays for enhancing cardiac drug testing on hipsc-cms heterogeneous tissues. *Journal of Physiology*, 2025.

[4] Sofia Botti, Chiara Bartolucci, Claudia Altomare, Michelangelo Paci, Lucio Barile, Rolf Krause, Luca Franco Pavarino, and Stefano Severi. A novel ionic model for matured and paced atrial-like human iPSC-CMs integrating Ikur and IKCa currents. *Computers in Biology and Medicine*, 180:108899, 2024. ISSN 0010-4825. https://doi.org/10.1016/j.compbiomed.2024.108899.

[5] Piero Colli Franzone, Luca Franco Pavarino, and Simone Scacchi. *Mathematical Cardiac Electrophysiology*. Springer, 2014. ISBN 978-3-319-04801-7.

[6] Jordan Elliott, Luca Mainardi, and Jose Rodriguez. Cellular heterogeneity and repolarisation across the atria: an in silico study. *Medical and Biological Engineering and Computing*, 60, 09 2022. 10.1007/s11517-022-02640-x.

[7] Marco Favino, Sonia Pozzi, Simone Pezzuto, Frits W. Prinzen, Angelo Auricchio, and Rolf Krause. Impact of mechanical deformation on pseudo-ecg: a simulation study. *EP Europace*, 18(suppl_4):iv77–iv84, 12 2016. ISSN 1099-5129. 10.1093/europace/euw353.

[8] Herbert M Himmel, Alexandra Bussek, Michael Hoffmann, Rolf Beckmann, Horst Lohmann, Matthias Schmidt, and Erich Wettwer. Field and action potential recordings in heart slices: correlation with established in vitro and in vivo models. *British Journal of Pharmacology*, 166(1):276–296, 2012. https://doi.org/10.1111/j.1476-5381.2011.01775.x.

[9] D. C. Kernik, S. Morotti, H. Wu, P. Garg, H. J. Duff, J. Kurokawa, J. Jalife, J. C. Wu, E. Grandi, and C. E. Clancy. A computational model of induced pluripotent stem-cell derived cardiomyocytes incorporating experimental variability from multiple data sources. *The Journal of Physiology*, 597(17):4533–4564, 2019.

[10] J. T. Koivumäki, N. Naumenko, T. Tuomainen, J. Takalo, M. Oksanen, K.J. Puttonen, S. Lehtonen, J. Kuusisto, M. Laakso, J. Koistinaho, and P. Tavi. Structural immaturity of human iPSC-derived cardiomyocytes: In silico investigation of effects on function and disease modeling. *Frontiers in Physiology*, 9, 2018. ISSN 1664-042X.

[11] S. Kussauer, R. David, and H. Lemcke. hipscs derived cardiac cells for drug and toxicity screening and disease modeling: What micro- electrode-array analyses can tell us. *Cells*, 8, 2019. 10.3390/cells8111331.

[12] Marta Lemme, Bärbel M. Ulmer, Marc D. Lemoine, Antonia T.L. Zech, Frederik Flenner, Ursula Ravens, Hermann Reichenspurner, Miriam Rol-Garcia, Godfrey Smith, Arne Hansen, Torsten Christ, and Thomas Eschenhagen. Atrial-like engineered heart tissue: An in vitro model of the human atrium. *Stem Cell Reports*, 11(6):1378–1390, 2018. ISSN 2213-6711. https://doi.org/10.1016/j.stemcr.2018.10.008.

[13] A. M. Lodrini, L. Barile, M. Rocchetti, and C. Altomare. Human induced pluripotent stem cells derived from a cardiac somatic source: Insights for an in-vitro cardiomyocyte platform. *International Journal of Molecular Sciences*, 21(2), 2020. ISSN 1422-0067.

[14] CÉline Moulin, Alain Gliere, Daniel Barbier, Sebastien Joucla, Blaise Yvert, Pascal Mailley, and Régis Guillemaud. A new 3-D finite-element model based on thin-film approximation for microelectrode array record-

ing of extracellular action potential. *IEEE Transactions on Biomedical Engineering*, 55(2):683–692, 2008. 10.1109/TBME.2007.903522.

[15] Petra Mulder, Tessa de Korte, Elena Dragicevic, Udo Kraushaar, Richard Printemps, Maria L.H. Vlaming, Stefan R. Braam, and Jean-Pierre Valentin. Predicting cardiac safety using human induced pluripotent stem cell-derived cardiomyocytes combined with multi-electrode array (MEA) technology: A conference report. *Journal of Pharmacological and Toxicological Methods*, 91:36–42, 2018. ISSN 1056-8719. https://doi.org/10.1016/j.vascn.2018.01.003.

[16] H. Ni and Eleonora Grandi. Computational modeling of cardiac electrophysiology. *Methods in molecular biology*, 2735:63–103, 2023. 10.1007/978-1-0716-3527-8_5.

[17] M. Paci, E. Passini, A. Klimas, S. Severi, J. Hyttinen, B. Rodriguez, and E. Entcheva. All-optical electrophysiology refines populations of in silico human iPSC-CMs for drug evaluation. *Biophysical Journal*, 118(10):2596–2611, 2020. ISSN 0006-3495.

[18] Michelangelo Paci, Risto-Pekka Pölönen, Dario Cori, Kirsi Penttinen, Katriina Aalto-Setälä, Stefano Severi, and Jari Hyttinen. Automatic optimization of an in silico model of human iPSC derived cardiomyocytes recapitulating calcium handling abnormalities. *Frontiers in Physiology*, 9(JUN), 2018. 10.3389/fphys.2018.00709.

[19] Robert S. Pickard. A review of printed circuit microelectrodes and their production. *Journal of Neuroscience Methods*, 1:301–318, 1979. URL `https://api.semanticscholar.org/CorpusID:5634904`.

[20] Pallavi Pushp, Diogo E S Nogueira, Carlos A V Rodrigues, Frederico C Ferreira, Joaquim M S Cabral, and Mukesh Kumar Gupta. A concise review on induced pluripotent stem cell-derived cardiomyocytes for personalized regenerative medicine. *Stem cell reviews and reports*, 17(3):748—776, June 2021. ISSN 2629-3269. 10.1007/s12015-020-10061-2.

[21] Luca Sala, D. Ward van Oostwaard, L. Tertoolen, C. Mummery, and M. Bellin. Electrophysiological analysis of human pluripotent stem cell-derived cardiomyocytes (hpsc-cms) using multi-electrode arrays (meas). *Journal of Visualized Experiments : JoVE*, 2017. 10.3791/55587.

[22] Francesca Simone, Alessandro Trancuccio, Jaroslaw Karol Sochacki, Celia Martínez Prieto, Silvia G. Priori, Luca F. Pavarino, and Demetrio J. Santiago. A novel computational model of human ipsc-derived ventricular myocytes with improved l-type calcium current for application to timothy syndrome. *Scientific Reports*, Feb 2026. ISSN 2045-2322. 10.1038/s41598-026-37707-4.

[23] Micha E Spira and Aviad Hai. Multi-electrode array technologies for neuroscience and cardiology. *Nature nanotechnology*, 8(2):83—94, February 2013. ISSN 1748-3387. 10.1038/nnano.2012.265.

[24] Joakim Sundnes, Glenn Terje Lines, Xing Cai, Bjørn Frederik Nielsen, Kent-Andre Mardal, and Aslak Tveito. *Computing the Electrical Activity in the Heart*, volume 1. Springer Science & Business Media, 2007. ISBN 978-3-540-33437-8.

[25] K. Takahashi and S. Yamanaka. Induction of pluripotent stem cells from mouse embryonic and adult fibroblast cultures by defined factors. *Cell*, 126(4):663–676, aug 2006.

[26] L. Tertoolen, S. Braam, B. V. Meer, R. Passier, C. Mummery, and C. Mummery. Interpretation of field potentials measured on a multi electrode array in pharmacological toxicity screening on primary and human pluripotent stem cell-derived cardiomyocytes. *Biochemical and Biophysical Research Communications*, 497:1135 – 1141, 2017. 10.1016/j.bbrc.2017.01.151.

[27] Eliott Tixier, Fabien Raphel, Damiano Lombardi, and Jean-Frédéric Gerbeau. Composite biomarkers derived from micro-electrode array measurements and computer simulations improve the classification of drug-induced channel block. *Frontiers in Physiology*, Volume 8 - 2017, 2018. ISSN 1664-042X. 10.3389/fphys.2017.01096.

[28] Natalia A. Trayanova, A. Lyon, J. Shade, and Jordi Heijman. Computational modeling of cardiac electrophysiology and arrhythmogenesis: toward clinical translation. *Physiological Reviews*, 104:1265 – 1333, 2023. 10.1152/physrev.00017.2023.

[29] Z Wang, B Fermini, and S Nattel. Sustained depolarization-induced outward current in human atrial myocytes. evidence for a novel delayed rectifier K+ current similar to Kv1.5 cloned channel currents. *Circulation Research*, 73(6):1061–1076, 1993. 10.1161/01.RES.73.6.1061.

[30] Erich Wettwer, Ottó Hála, Torsten Christ, Jürgen F. Heubach, Dobromir Dobrev, Michael Knaut, András Varró, and Ursula Ravens. Role of IKur in controlling action potential shape and contractility in the human atrium. *Circulation*, 110(16):2299–2306, 2004. 10.1161/01.CIR.0000145155.60288.71.

[31] Yankun Yu, Mengrong Zhang, Ren Chen, Feng Liu, Pengfei Zhou, Lei Bu, Ying Xu, and Lei Zheng. Action potential response of human induced-pluripotent stem cell derived cardiomyocytes to the 28 cipa compounds: A non-core site data report of the cipa study. *Journal of Pharmacological and Toxicological Methods*, 98:106577, 2019. ISSN 1056-8719. https://doi.org/10.1016/j.vascn.2019.04.003.

Supplementary Files

This is a list of supplementary files associated with this preprint. Click to download.

- supplementarymaterial.pdf